New Journal of Physics
The open access journal at the forefront of physics

Deutsche Physikalische Gesellschaft DPG IOP Institute of Physics

PAPER • OPEN ACCESS

Nitric oxide density distributions in the effluent of an RF argon APPJ: effect of gas flow rate and substrate

To cite this article: S Iseni *et al* 2014 *New J. Phys.* **16** 123011

View the article online for updates and enhancements.

Related content

- The kINPen—a review on physics and chemistry of the atmospheric pressure plasma jet and its applications
- Numerical analysis of the effect of nitrogen and oxygen admixtures on the chemistry of an argon plasma jet operating at atmospheric pressure
- ***In situ*** absolute air, O_3 and NO densities in the effluent of a cold RF argon atmospheric pressure plasma jet obtained by molecular beam mass spectrometry

Recent citations

- Description of the physicochemical properties of a gas–liquid phase discharge under the Ar—N2 environment
H. I. A. Qazi *et al*
- Modelling of turbulent reacting flow for a cold atmospheric pressure argon plasma jet
I L Semenov and K-D Weltmann
- Mechanistic aspects of plasma-enhanced catalytic methane decomposition by time-resolved *operando* diffuse reflectance infrared Fourier transform spectroscopy
S Zhang *et al*

This content was downloaded from IP address 194.95.157.48 on 29/09/2020 at 09:17

New Journal of Physics
The open access journal at the forefront of physics
Deutsche Physikalische Gesellschaft DPG | IOP Institute of Physics

Nitric oxide density distributions in the effluent of an RF argon APPJ: effect of gas flow rate and substrate

S Iseni[1,2], S Zhang[3], A F H van Gessel[3], S Hofmann[3], B T J van Ham[3], S Reuter[1,2], K-D Weltmann[2] and P J Bruggeman[3,4]

[1] Center for Innovation Competence plasmatis, 17489 Greifswald, Germany
[2] Leibniz Institute for Plasma Science and Technology (INP), 17489 Greifswald, Germany
[3] Eindhoven University of Technology, Department of Applied Physics, PO Box 513, 5600 MB, Eindhoven, The Netherlands
[4] Department of Mechanical Engineering, University of Minnesota, 111 Church Street SE, Minneapolis, MN 55455, USA
E-mail: pbruggem@umn.edu

Received 27 July 2014, revised 4 October 2014
Accepted for publication 30 October 2014
Published 2 December 2014

New Journal of Physics **16** (2014) 123011

doi:10.1088/1367-2630/16/12/123011

Abstract

The effluent of an RF argon atmospheric pressure plasma jet, the so-called kinpen, is investigated with focus on the nitric-oxide (NO) distribution for laminar and turbulent flow regimes. An additional dry air gas curtain is applied around the plasma effluent to prevent interaction with the ambient humid air. By means of laser-induced fluorescence (LIF) the absolute spatially resolved NO density is measured as well as the rotational temperature and the air concentration. While in the laminar case, the transport of NO is attributed to thermal diffusion; in the turbulent case, turbulent mixing is responsible for air diffusion. Additionally, measurements with a molecular beam mass-spectrometer (MBMS) absolutely calibrated for NO are performed and compared with the LIF measurements. Discrepancies are explained by the contribution of the NO_2 and N_2O to the MBMS NO signal. Finally, the effect of a conductive substrate in front of the plasma jet on the spatial distribution of NO and air diffusion is also investigated.

Content from this work may be used under the terms of the Creative Commons Attribution 3.0 licence. Any further distribution of this work must maintain attribution to the author(s) and the title of the work, journal citation and DOI.

© 2014 IOP Publishing Ltd and Deutsche Physikalische Gesellschaft

Keywords: atmospheric pressure plasma jets, nitric oxide, laser induced fluorescence, molecular beam mass spectrometry, spectroscopy, plasma medicine

1. Introduction

Due to the various advantages of atmospheric pressure plasmas compared to low pressure plasmas, a strong interest in these discharges is growing which opens up new fields in plasma technology [1, 2]. One of these fields is known as plasma medicine which is aiming to combine room temperature atmospheric pressure plasmas with living matter and clinical medicine [3, 4]. Different applications are currently under investigation since plasma appears to be a promising tool for decontamination and an alternative to the usual chemical approaches to the inactivation of pathogens [5–7]. Additionally, it has been observed that plasma treatments may lead to improved wound healing e.g. in chronic wound treatments [8–10]. Various plasma agents, such as (V)UV radiation, electric field, charges and reactive oxygen and nitrogen species (RONS), can influence cells and tissues. Especially reactive species such as hydrogen peroxide (H_2O_2) or nitric-oxide (NO) are known to induce effects on cells and tissues [11–14]. While NO is toxic at higher concentration ($2.5 \times 10^{13}\,cm^{-3}$) it triggers cell signaling and biological mechanisms at low concentrations as reported in the monograph of Lancaster and references therein [15]. The generation of NO by atmospheric pressure plasmas and its diagnostics have been investigated for different kinds of plasma devices, operating with helium and argon with an admixture of air [16–21].

In this work, the spatial distribution of NO from a radio-frequency (RF) argon atmospheric pressure plasma jet is investigated. The present work builds on the previous research of van Gessel *et al* [16] and aims to study the influence on the NO density profiles within the effluent and near field of the plasma jet with different flow patterns. Recently, it has been shown by Iseni *et al* [22] and Robert *et al* [23] that in such plasma jet devices, discharge propagation and gas flow pattern are strongly correlated. Consequently, an effect of the reactive species generation is anticipated. In this work, both laminar and turbulent flow regimes are investigated. Moreover, the plasma jet is equipped with an additional cap allowing for the supply of an external gas as a curtain around the plasma jet effluent [24]. The influence of this gas curtain on the distribution of NO is presented. The gas temperature of the plasma effluent is measured by LIF [17] to interpret the results. The influence of a metal substrate on the NO density distribution which also has an effect on the flow pattern in the effluent will be presented for varying conditions. The use of a substrate close to the region of interest requires us to take into consideration technical issues such as optical vignetting. Additionally, the influence of the flow regime and the air entrainment into the effluent is deduced from the decay time of the fluorescence which is determined by the collisional quenching of the NO(A) state by Ar and air.

Two different techniques used in the present work, laser-induced fluorescence (LIF) and molecular beam mass spectrometer (MBMS), have been used in previous publications for the determination of absolute NO densities [25]. Nevertheless, the comparison of both diagnostics was performed at different orientation of the plasma jet which led to uncertainties on the origin of the discrepancies found between the two methods. The present work re-investigates the NO densities at comparable conditions and additional observations and conclusions are presented. The previous work of Iseni *et al* [26] dealing with the absolute density of nitric dioxide (NO_2)

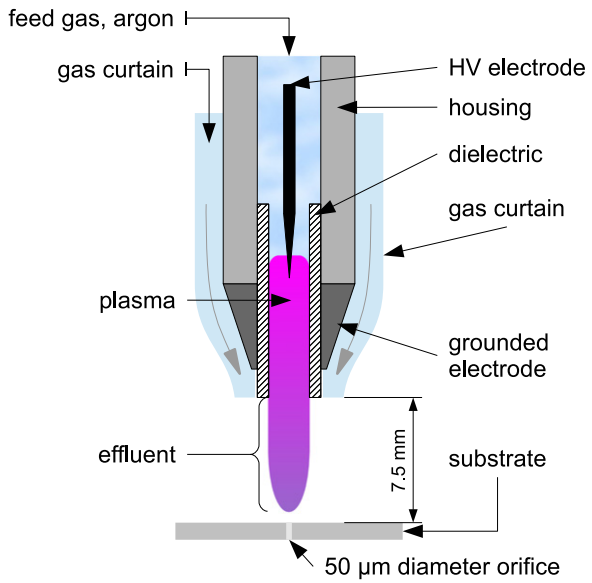

Figure 1. Schematic of the plasma jet (kinpen) and the implementation of the gas curtain around the effluent [3, 24]. A metal substrate resembling the MBMS sampling plate with a 50 μm diameter orifice is positioned at a distance of 7.5 mm from the jet nozzle.

as well as literature data are used to discuss the proposed non-selectivity of the mass spectrometer measurement in more detail.

2. Experimental setup

2.1. Plasma source

The cold non-equilibrium atmospheric-pressure argon discharge investigated in this work is the commercially available device kinpen (neoplas GmbH, Germany) [3]. It is driven with a 1 MHz radio frequency (RF) electric excitation. Figure 1 illustrates the basic geometrical and electrical configuration which consists of a high-voltage (HV) needle electrode centered within a 1.6 mm dielectric capillary. An RF continuous voltage with an amplitude between 2–6 kV is applied to the needle. The jet is driven at an RF power between 0.9–2.2 W and operates with a flow rate between 0.5–3.0 slm dry argon. The typical argon luminous effluent length is between 10–15 mm and depends on the input power and impurities such as air or water but is independent of the flow rate. Admixtures of molecular oxygen and nitrogen within the feed gas are possible up to 2.0%. However, the molecular admixtures significantly reduce the effluent length from about 15 mm to a few millimeters. In this work, 1.0% of dry air is admixed to the argon in order to prevent any fluctuation with the nitric oxide production due to potentially varying air impurities of the argon feed gas.

In order to control the interaction of the effluent with the surrounding atmosphere, an external gas flow is applied through a concentric cylindrical channel of the jet nozzle. More information can be found e.g. in [24]. This gas shroud can be fed with different gases and prevents the diffusion of ambient humid air into the effluent for particular flow conditions [27]. Consequently, the gas curtain can enhance the reproducibility and the stability of the treating

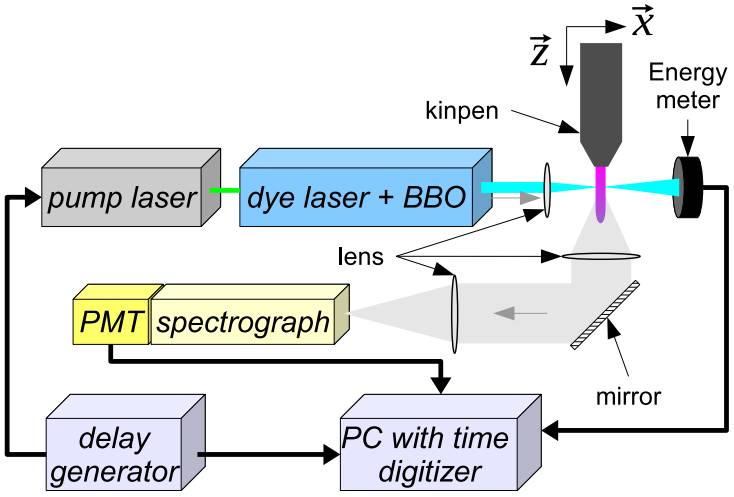

Figure 2. Experimental setup of the LIF diagnostic applied to the kinpen.

conditions by excluding any variation of surrounding humid air which can vary from lab to lab around the world. Furthermore, a choice of gas used for the curtain allows influencing of the effluent chemistry and may be an additional tunable parameter to adjust plasma treatments [24]. During all the experiments, the plasma device is operated vertically, with the gas flow in the direction of the gravitational field.

2.2. Laser-induced fluorescence of NO

LIF of NO is a standard technique in the combustion community [28]. LIF has been applied to investigate plasma discharges such as the process mechanism used to remove pollutants with positive streamers [29]. Thanks to fundamental studies on the NO energy structure (initiated in the combustion community) the spectroscopic constants are well known [30]. The experimental setup used in this work (see figure 2) is identical to the one introduced by van Gessel *et al* [17]. The most important aspects of the system are described and the reader is referred for more details to the latter reference. The excitation of the rotational transition NO(A-X)(0–0) is obtained by using a frequency doubled tunable dye laser system (Cobra, Sirah Laser und Plasmatechnik GmbH, Germany) around 226.2 nm with Coumarin 2 as a dye. The latter is pumped at 355 nm by a high repetition rate Nd:YAG laser operating at 1.0 kHz (IS6III-E, EdgeWave GmbH, Germany). The typical pulse energy is measured to range between 2.5–3.5 μJ with pulse-to-pulse fluctuations of about 1.0 μJ and a pulse duration of 6 ns FWHM. The energy variation is corrected for in post-processing with regards to the synchronized data from the detector and the laser energy meter. The laser beam is focused with a lens to a 200 μm diameter spot aligned with the radial center of the jet nozzle. Focusing the beam maintains sufficient spatial resolution compared to the 1.6 mm diameter of the capillary. The fluorescence intensity was checked to be proportional to the laser pulse energy and confirms that no saturation of the transition occurs [17]. The fluorescence is collected and imaged on the entrance slit of a 0.2 m monochromator (model 234/302, McPherson Inc., USA) by two 200 mm quartz lenses. A spectral resolution of 0.2 nm FWHM is reached with a 1200 groove mm^{-1}grating. With a nominal dispersion of 4.0 $nm \cdot mm^{-1}$, the bandwidth is set at 12.0 nm centered at 247.0 nm which allows a recording of the full rotational band NO(A-X)(0–2). The signal at the output of the monochromator is detected by a photomultiplier (model R8486,

Hamamatsu, Japan) operating in photon-counting mode and read out via a 1.0 GHz sampling rate digitizer card connected to a computer.

The laser linewidth allows us to resolve a single rotational transition, thus the total NO(X) density needs to be obtained by the knowledge of the Boltzmann factor (f_B) [17]. Hence, correcting for the temperature is important and different approaches are suitable, such as e.g. resorting to Rayleigh scattering [16]. However, here the approach of van Gessel *et al* is followed to excite a small band of transitions of which the total fluorescence is quasi-independent of the temperature [16] in the investigated temperature range. Indeed, for temperatures included within the range from 300–600 K, which is the case in this work, integrating the fluorescence signal resulting from the excitation wavelength scan from 226.23–226.28 nm ($P_1(4)$, $P_1(5)$, $P_1(12)$, $Q_2(16)$, $Q_{12}(16)$ and $R_2(11)$[5]) provides a temperature dependence of the fluorescence intensity below 3% . Hence, for each measurement, an excitation wavelength scan is performed from 226.225–226.280 nm with a scan speed of 0.42 pm $\cdot$ s^{-1} and the LIF signal results as the sum of the fluorescence intensity of the stated transitions.

Collisional quenching with other particles, such as argon and air, reduces significantly the fluorescence intensity; however, these fluorescence losses are taken into consideration according to the relation $\tau_{\mathrm{det}} = (A_{\mathrm{tot}} + Q)^{-1}$, with τ_{det} being the recorded decay time of the fluorescence, A_{tot} being the spontaneous emission coefficient of the whole vibrational band and Q the collisional quenching rate in the unit of s^{-1}.

To determine the ground state NO(X) density, a simplified two-level energy scheme of NO is considered and leads to the following rate equation,

$$\frac{\mathrm{d}n_{\mathrm{u}}}{\mathrm{d}t} = B_{\mathrm{lu}} I(t) n_{\mathrm{l}} - \left(A_{\mathrm{tot}} + Q\right) n_{\mathrm{u}}, \tag{1}$$

where the subscript u and l refer to the upper and lower energy levels of the molecule respectively, n_x (m^{-3}) is the population density of an energy level x, B_{lu} (m$^{-2} \cdot$ J$^{-1} \cdot$ s^{-1}) is the absorption coefficient from the lower to the upper state, $A_{\mathrm{tot}} = \sum_l A_{\mathrm{ul}} = \frac{1}{\tau_0}$ (s^{-1}) is the sum over all the transitions from the upper to the lower state. Stimulated emission from the upper to the lower state is neglected since the laser fluence is small and only a minor fraction of NO(X) state is excited. $I(t)$ (J $\cdot$ m^{-2}) is the laser intensity defined as,

$$I(t) = \frac{E_{\mathrm{I}} \Gamma}{a} i(t) \tag{2}$$

with E_{I} (J) being the energy of the pulse, Γ (s) being the overlap integral and a (m^2) the laser spot area. More information about the definition and the characterization of the overlap integral Γ can be found in [31] and references therein. $i(t)$ (s^{-1}) is the temporal shape of the laser pulse normalized to the area as $\int_{-\infty}^{+\infty} i(t)\mathrm{d}t = 1$. The relation between the integrated LIF signal S and the NO(X) density n_{gnd} can be deduced from equation (1):

$$S = n_{\mathrm{gnd}} C \frac{V}{a} E_{\mathrm{I}} \cdot \frac{A_{\mathrm{det}}}{A_{\mathrm{u}} + Q} \cdot B_{\mathrm{lu}} f_{\mathrm{B}} \tag{3}$$

where V (m^{-3}) is the sampled volume, C is a dimensionless factor characterizing the optical efficiency of the collection optics including the quantum efficiency of the detector, A_{det} (s^{-1}) is a sum of the Einstein coefficients over all allowed rotational transitions and f_{B} refers to the

[5] The transitions are denominated here with the Hund's case b.

Boltzmann factor. More details can be found in [17]. The absolute calibration of the laser induced fluorescence measurement is described in section 3.2.

2.3. Molecular beam mass spectrometer (MBMS)

The study of the NO production and distribution in the jet effluent by LIF is complemented with mass spectrometry. Here, a molecular beam mass spectrometer (EPIC/IDP Series 1000, Hiden Analytical Ltd, Warrington, UK) is used as previously introduced in [6, 25]. It consists of a quadrupole mass spectrometer (QMS) coupled to a home-made three stage pressure reduction system. The sampling orifice has a diameter of 50 μm. The reader is referred to [25] for a sketch of the sampling stage and all details. A cylinder of 80 mm diameter, 43 mm hight is mounted on the sampling plate and centered with the orifice. An exhaust ring is implemented in the bottom of this cup-like cylinder in order to prevent accumulation of argon and advantageously influence the partial pressure of air to not saturate the cup with argon, thus preventing artificial change of the plasma chemistry. The exhaust system is powered by a pump and a rotameter to adjust the exhaust rate (typically 30 slm). The three stage pressure reduction system is operated at 10^{-3} mbar, 10^{-6} mbar and 10^{-8} mbar respectively. A Bessel box is installed within the third chamber in front of the QMS to prevent UV and V-UV radiation from the plasma reaching the detector. In this work, the ionization source is tuned to generate electrons with a maximum energy peak at 70 eV. This is necessary to have a signal which is significantly larger compared to the detection limit. The high ionization energy causes higher energetic electron inducing dissociative ionization processes which will require additional efforts to analyze the data. Consequently, heavier molecules will be partially dissociated into lighter ones and thus reduce the number count at their original mass. These so-called cracking patterns are described and tabulated in the literature and are used to analyze data and correct for the species density [32]. For instance, molecules like N_xO_y will contribute significantly to the NO mass count with a known ratio. Unfortunately, threshold ionization potential measurement did not yield a signal above the detection limit for NO under the present experimental condition. During the calibration procedure [25] as well as the measurements, the plasma jet is positioned vertically, the flow oriented parallel to the gravitational force. With 1.0% of air admixed, the effluent length is shorter than with pure argon. The capillary tip is set accurately 7.5 mm away from the orifice in order to avoid attachment of the plasma with the metallic surface of the MBMS. The latter case will strongly influence the plasma which tends to a filamentary discharge which could interact with the orifice [33]. In the frame of this work, NO and O_3 densities are investigated for different radial positions of the plasma jet.

3. Measurement and calibration procedures

3.1. Rotational temperature of NO(X)

The determination of the gas temperature of atmospheric plasma discharges can pose a challenge since those plasmas are far from thermodynamic equilibrium. However, several interpretations and experimental approaches have led to accurate gas temperature estimations [34]. It is reported that the NO(A) rotational temperature leads to an overestimation of the gas temperature at elevated gas temperatures, $T_g > 1000$ K [35]. Similar issues are presented for $N_2(C)$ in an argon mixture due to the near resonant excitation of $N_2(C)$ by Ar metastable atoms

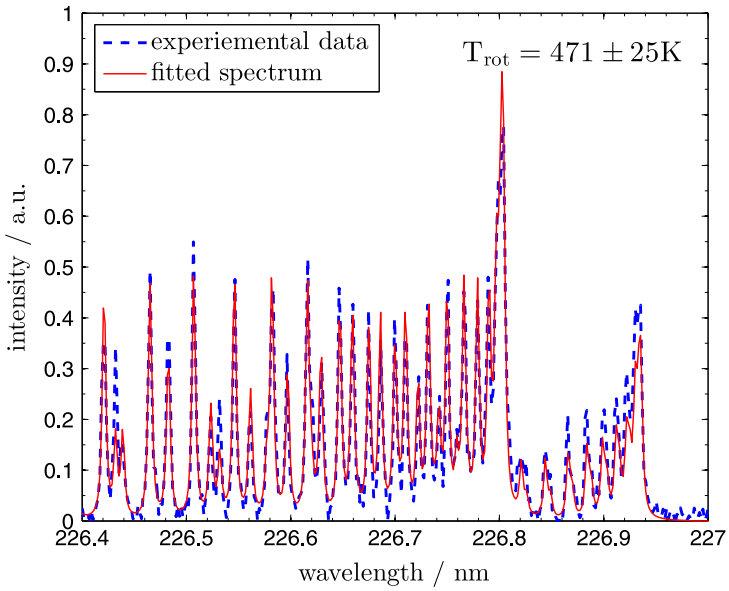

Figure 3. Experimental NO(A-X)(0–0) LIF excitation spectrum collected from the plasma effluent at 3.0 mm from the nozzle operating under laminar flow conditions (1.0 slm). The rotational temperature resulting from the fit is 471 ± 25 K.

Table 1. Comparison of different parameters for three fixed positions in the effluent and far field area for laminar and turbulent conditions. No gas curtain is used except for †.

	laminar $Re = 930$			turbulent $Re = 2790$		
ax. pos./mm	0	3	7	0	3	7
gas temp./K	521 ± 32	471 ± 25	447 ± 23	432 ± 28	418 ± 20	424 ± 37
gas temp.†/K	476 ± 24	448 ± 22	433 ± 31	—	—	—
Q / 10^7 s^{-1}	1.64	1.89	6.80	1.80	2.30	7.69
[NO]/10^{19} m^{-3}	30	20	7	19	5.9	1.9
[air]/10^{23} m^{-3}	6.1	7.2	27	6.4	8.0	56

[36]. To this end NO(X) rotational temperature by LIF is used to measure the gas temperature in the jet. Figure 3 illustrates an example of a rotational spectrum resulting from a wavelength scan from 226.4–227.0 nm. The fitting algorithm introduced by van Gessel *et al* [37] is used to fit the ro-vibrational spectrum. In practice, a high spectral resolution from the laser (typically 2.0 pm) is essential in order to decrease the uncertainties induced by the fit routine. Due to the time consuming nature of the measurement, measurements have only been performed o*n*-axis. The results are presented in the table 1 in section 4.1.2.

3.2. Absolute NO(X) density from LIF and vignetting correction

The absolute calibration of the NO fluorescence is performed as described by van Gessel *et al* [16]. Briefly, a mixture of argon and 10.0 ppm NO ($n_{calib.} = 2.45 \times 10^{20}$ m^{-3}) flows through the 1.6 mm inner diameter capillary at a flow rate of 1.0 slm. The fluorescence is induced from the laser spot position located at the tip of the jet nozzle (axial position at 0.5 mm) and the central radial position where the density of NO is assumed to remain constant. At this position with a non-turbulent flow, dilution of the mixture due to surrounding air is negligible [22]. The

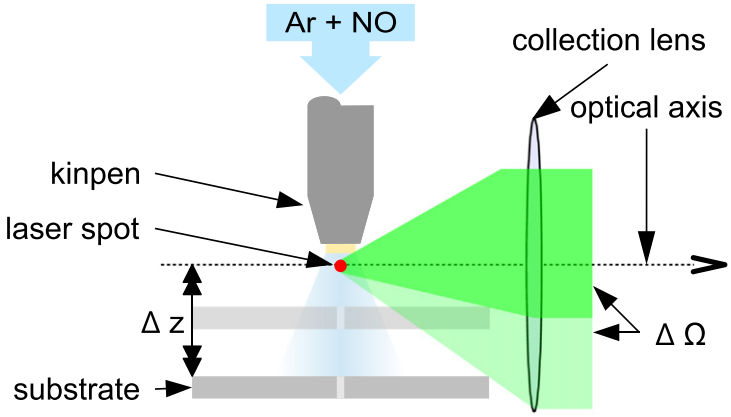

Figure 4. Scheme of the experimental method used to perform the absolute NO density calibration and the correction of the vignetting. The vertical position of the substrate, z, is set as a parameter for the vignetting correction.

absolute density of NO(X) can be expressed as follows,

$$n_{\mathrm{NO(X)}} = \frac{S}{E\tau} \cdot \left[\frac{n_{\mathrm{calib.}} E_{\mathrm{calib.}} \tau_{\mathrm{calib.}}}{S_{\mathrm{calib.}}} \right] \tag{4}$$

where n_{x} is the density of the particle x (m^{-3}), S ($\mathrm{J \cdot m}^{-2}$) refers to the time integrated LIF signal, E (J) is the laser pulse energy and τ (s) is the decay time of the fluorescence. However, the presence of a large substrate (compared to the effluent size) in our experiment induces additional complexity. The main one is *vignetting* and results in a variation of the collection solid angle close to the substrate. The latter masks a fraction of the photon flux coming from the sampled volume, which reaches the monochromator slit. As a consequence, the vignetting directly depends on the vertical position of the substrate. The substrate has a much larger diameter compared to the horizontal variation of the measurement thus the vignetting only depends on the axial portion in this case. Consequently, the translation ΔZ of the substrate compared to the jet nozzle induces a variation of the varying solid angle $\Delta\Omega$ (as illustrated in figure 4) which has to be characterized for each vertical position. By adding a known concentration of NO to the argon feed gas, it is possible to quantify the amount of fluorescence due to vignetting by the substrate. Figure 4 illustrates how the absolute calibration of the NO signal is performed including the vignetting artifact. The plasma jet is set vertically, with the tip of the capillary nozzle aligned 0.5 mm above the optical axis which is defined as the vertical origin. The laser beam is pointed to cross the optical axis perpendicularly and adjusted to the center of the capillary where the NO density remains constant. The substrate, mounted on a post with a vertical micrometer translation adjustment screw, is positioned in front of the jet nozzle. The fluorescence is then collected for different vertical positions of the substrate from 0.5–7.5 mm on the optical axis with an increment of 0.5 mm. Consequently, a relation between ΔZ and S (involving $\Delta\Omega$ and the geometry of the substrate) is, thus, experimentally determined and yields a correction factor of the vignetting plotted in figure 5. Equation (3) can be re-writen as,

$$n_{\mathrm{gnd}} = \zeta \cdot \frac{S \cdot a}{CVE_{\mathrm{I}}} \cdot \frac{A_{\mathrm{u}} + Q}{A_{\mathrm{det}}} \tag{5}$$

with ζ the vignetting correction factor. From figure 5, it can be seen that the characterization of the vignetting corrects up to a factor 2 in the photon counts which would lead to a significant

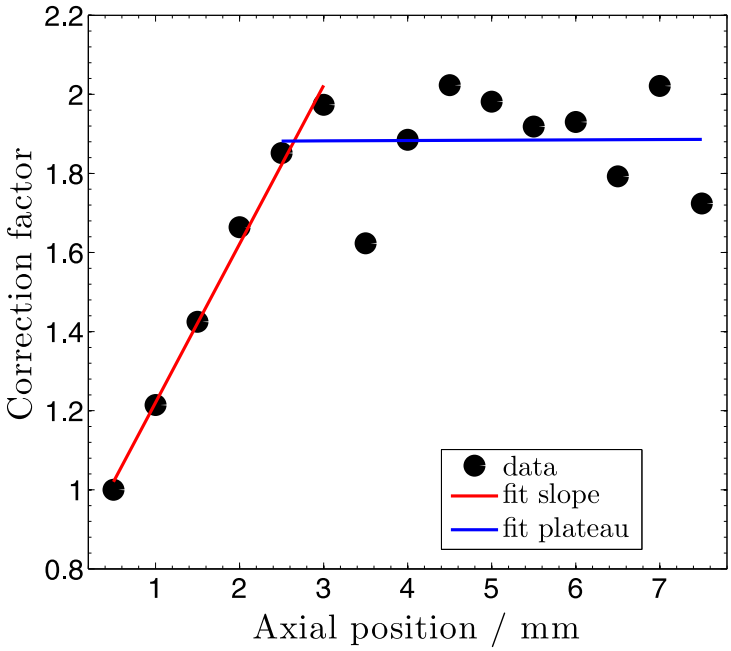

Figure 5. Map of the vignetting correction factor ζ for the investigated domain. The origin of the graph corresponds to the nozzle tip of the capillary and the position of the plate is 7.5 mm.

underestimation of the NO(X) density. The variation in the correction factor suggests an accuracy of about 25% . The reproducibility of the measurement has been determined to be 20% . Thus the total error on the vignetting measurements are estimated to be 45% .

3.3. Determination of air density in the effluent

Due to the dependence of the effective lifetime τ of NO(A) on the gas mixture due to quenching, it is possible to determine absolutely the air concentration diffusing into the effluent. From section 2.2, the detected decay time of the fluorescence signal can be defined as $\tau_{\mathrm{det}} = (A_{\mathrm{tot}} + Q)^{-1}$ with $Q = \sum_i k_{\mathrm{x}_i} n_{\mathrm{x}_i}$, n_{x} (m^{-3}) being the density of argon or air and k_{x} ($\mathrm{m}^3 \cdot \mathrm{s}^{-1}$) the rate coefficient of a reaction between NO(A) with a quencher x. Raiche *et al* report that the dependence of the NO(A) quenching rate coefficients of N_2 and O_2 are independent of the gas temperature between 300–750 K [38]. Moreover, Drake *et al* have published that Ar and NO quenching rate coefficients do not depend on the gas temperature in a range from 300–1750 K [39]. Additionally, the gas curtain may contain residual water vapor impurities. Consequently, the detected decay time, τ_{det}, can be expressed as,

$$\tau_{\mathrm{det}} = \frac{1}{A_{\mathrm{tot}} + \sum_i k_{\mathrm{x}_i} n_{\mathrm{x}_i}} = \frac{1}{A_{\mathrm{tot}} + k_{\mathrm{ar}} n_{\mathrm{ar}} + k_{\mathrm{air}} n_{\mathrm{air}} + k_{\mathrm{water}} n_{\mathrm{water}}}. \tag{6}$$

The calibration gas as described in section 3.2 allows us to determine the quenching rate of argon at room temperature. Indeed, $\tau_{\mathrm{calib}}^{-1} = A_{\mathrm{tot}} + k_{\mathrm{ar}} n_{\mathrm{ar}}$, hence the determination of $k_{\mathrm{ar}} = 3.5 \cdot 10^{-19}$ $\mathrm{m}^3 \cdot \mathrm{s}^{-1}$at 300 K and atmospheric pressure which is in good agreement with the literature ($3.9 \times 10^{-19}\,\mathrm{m}^3 \cdot \mathrm{s}^{-1}$ [40], $2 \times 10^{-19}\,\mathrm{m}^3 \cdot \mathrm{s}$ [41]). Furthermore, it is found from previous studies that water has a quenching rate coefficient three times higher than air ($k_{\mathrm{air}} = 2.96 \cdot 10^{-16}\,\mathrm{m}^3 \cdot \mathrm{s}^{-1}$ [17], $k_{\mathrm{water}} = 8.97 \cdot 10^{-16}$ $\mathrm{m}^3 \cdot \mathrm{s}^{-1}$ [41]) but as the water

concentration will never exceed 2% of the air concentration, in a good approximation the quenching by water can be neglected. The air density can be calculated with the following equation,

$$n_{\text{air}} = \frac{\tau_{\text{calib}} - \tau_{\text{det}}}{\tau_{\text{calib}}\,\tau_{\text{det}}\,k_{\text{air}}}. \tag{7}$$

The dissociation degree of O_2 in the effluent should be considered for high dissociation degrees. Fricke *et al* reported on an absolute atomic oxygen density of $2.5 \times 10^{20}\,\text{m}^{-3}$ for an admixture of 0.2% O_2 at 5 mm and 7 mm which corresponds to a dissociation degree of 0.25 % [42]. In order for O to be an important quencher, its quenching rate with NO(A) must be by a factor of a thousand higher than for air, which is highly unlikely. Therefore, the dissociation in the effluent has not taken influence into account for the fluorescence decay of NO(A).

3.4. MBMS calibration for nitric oxide and ozone

MBMS measurements also require an accurate calibration in order to reach absolute density determination. The absolute calibration of NO and O_3 is performed as presented in detail in [25]. Briefly, a known density of NO is applied at the entrance orifice of the MBMS similar to the conditions described for the LIF calibration. An identical procedure is realized for O_3 for which the molecules are generated via an ozone generator and the O_3 density is simultaneously measured by classical UV absorption. Concerning the accuracies, they have been determined to be in the order of 25 % including the reproducibility of the measurements. These are in agreement with the literature, e.g. Ellerweg *et al* reported an error of factor two on the data produced by their MBMS [43].

4. Results and discussions

The NO density profiles are presented as two dimensional color maps. The data is recorded with a sample step size of 250 μm and 500 μm in the radial (horizontal) and axial (vertical) direction respectively. The effect of the flow field, curtain flow, gas composition and the presence of a substrate are presented. In addition, MBMS data is compared with the LIF results.

4.1. Turbulent versus laminar flow

4.1.1. Spatial density distribution of NO. By increasing the feed gas flow rate a transition from a laminar to a turbulent flow regime in the effluent is induced. Earlier, Iseni *et al* reported that for this plasma jet geometry, the Reynolds number (*Re*) is 930 and 2790 for a feed gas flow rate of 1.0 slm and 3.0 slm respectively. The NO density distribution determined for the two different feed gas flow rates are mentioned above, with and without the presence of a gas curtain. The results are shown in figure 6. The corresponding gas temperatures are shown in table 1. The highest NO density is located at the tip of the nozzle. This is expected since most of the input energy is dissipated inside the dielectric capillary and it is thus anticipated that much of the NO is produced inside or close to the nozzle of the jet capillary. It could be that most of the NO is produced in a restricted area compared to the nozzle diameter (about 200 μm FWHM) and then diffuses into the effluent. The maximum NO density is not located on the axis of symmetry but is slightly shifted to one side by about 300 μm. This is not due to a misalignment of the visible plume to the laser beam, as the position of the maximum of NO density is found to

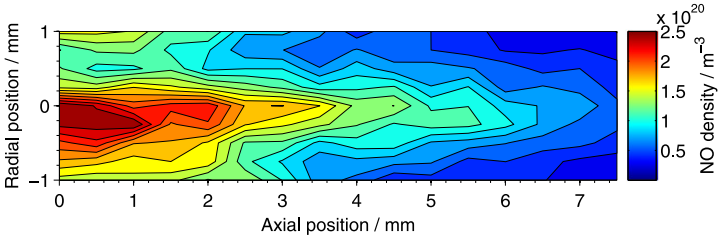

(a) Laminar flow, 1.0 slm argon + 1 % air, with gas curtain 1.6 slm

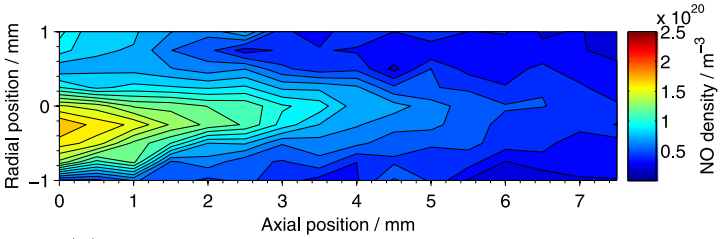

(b) Turbulent flow, 3.0 slm argon + 1 % air, no gas curtain.

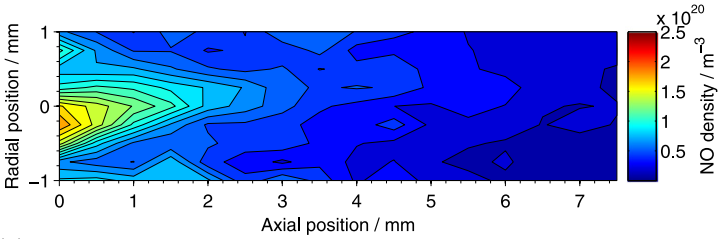

(c) Turbulent flow, the plasma jet fed with 3.0 slm argon + 1 % air and the gas curtain supplied with 5.0 slm dry air.

Figure 6. Absolute NO density profiles in the jet effluent. The laminar flow case with gas curtain (a) and the turbulent case without (b). (c) depicts the NO density profile for the turbulent case *with gas curtain*. The jet is free in air, without substrate and the plasma generator setup is kept constant.

be well correlated with the position of the plasma filament located within the capillary. Indeed, it was noticed during the experiment that the visible plasma effluent is not entirely homogeneous but a brighter filamentary area is observed. Note that in the laminar case the plasma filament is stable and often attached to the dielectric surface of the tube thus explaining the asymmetric NO production. As expected, the feed gas flow rate has an influence on the global NO density distribution. The NO density is larger for lower flow rates. This is explained, on one side, by a higher gas temperature (see table 1) due to a weaker heat dissipation. This is highly favorable to the NO production. Van Gaens *et al* have shown for similar conditions that the NO density is mainly determined by a local balance between production and destruction reactions in the early afterglow. In reference [44] the difference between the production and destruction rate is 10% at the position of maximum production rate. A moderate change in flow rate will have a limited effect on the NO density in the early afterglow. Moreover, an increase of the gas temperature strongly reduces the ozone production which is one of the key players in the destruction of NO [45]. On the other side, the residence time of N_2 and O_2 is larger for a lower flow rate which could enhance dissociation and chemical conversion in the discharge. In spite of a maximum NO density which is higher by a factor of about 1.5 in the laminar case than in the turbulent case, the density profiles are similar. Nonetheless, the NO density decays faster in the turbulent case. It is important to note that the length and the width of the plasma emission remain almost identical in both cases as shown in figure 7. Consequently, the volume of the

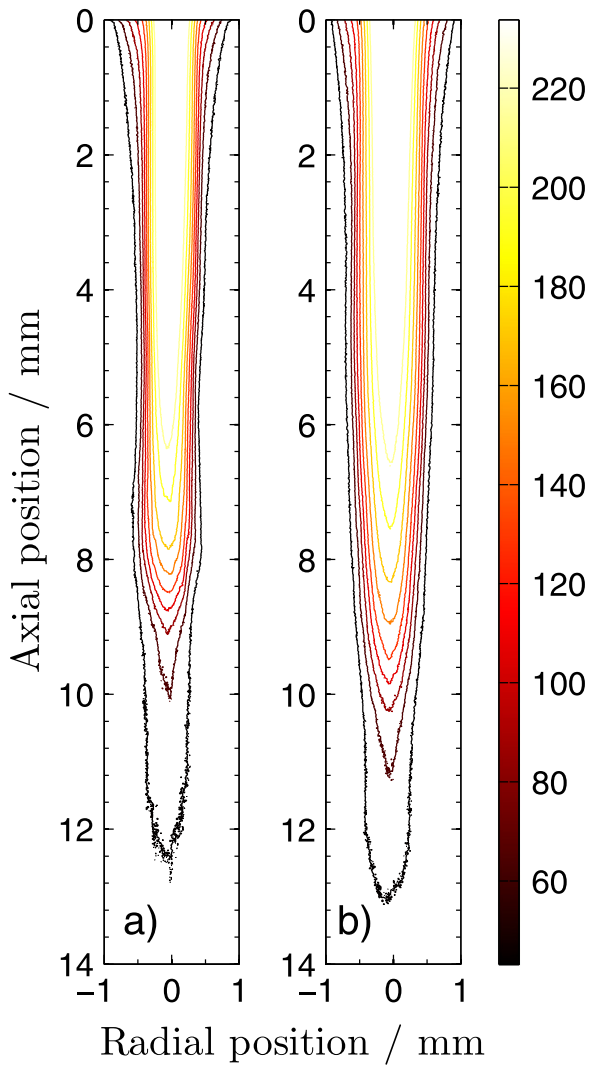

Figure 7. Comparison of the visible length of the effluent for 1.0 slm (a) and 3.0 slm (b) feed gas flow rate with 1.6 slm and 5.0 slm curtain gas flow rate respectively. The original data are grey-scaled photographs. Contour plots are chosen for a better readability and comparison.

afterglow is invariant and the spreading of NO is most likely due to a high mixing induced by the turbulence.

Recently, van Gaens *et al* reported from a computational simulation of a similar argon plasma source the main reactions responsible for the NO formation and destruction [44].

$$O + N_2(A) \rightarrow NO + N(^2D) \quad (8)$$

$$O + NO_2 \rightarrow NO + O_2 \quad (9)$$

Reactions (8) and (9) are identified to largely contribute to the NO production. NO molecules are mainly produced from atomic oxygen and the first metastable state of nitrogen rather than through Zeldovich mechanism [45]. The first reaction requires a high density of O and $N_2(A)$ which is inside the active plasma region and explains the higher NO density near the nozzle. In addition, a recycle reaction from NO_2 with O is important. Reaction (9) is dominant in the

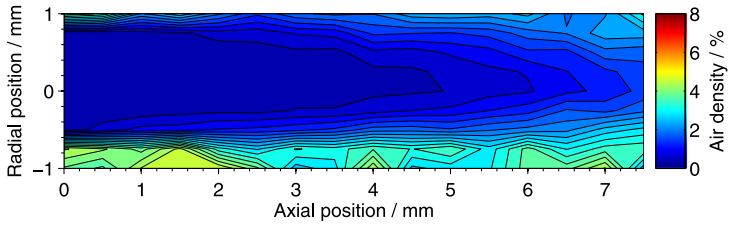

(a) Laminar flow, 1.0 slm argon + 1 % air with gas curtain 1.6 slm.

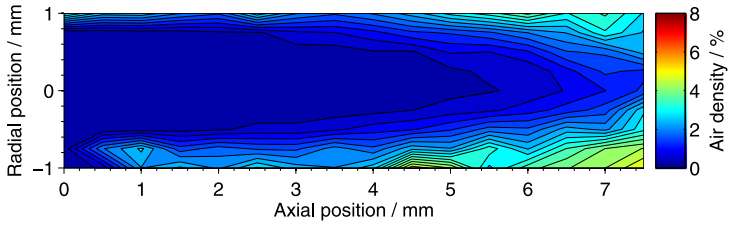

(b) Turbulent flow, 3.0 slm argon, no gas curtain.

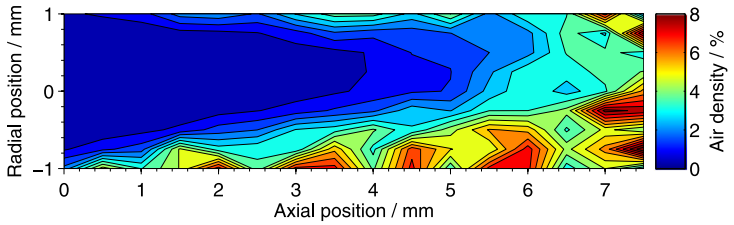

(c) Turbulent flow, 3.0 slm argon + 1 % air with gas curtain 5.0 slm.

Figure 8. Spatially-resolved air density distribution over the effluent and far field regions for 1.0 slm and 3.0 slm flow rate.

afterglow [44].

$$O + NO + M \rightarrow NO_2 + M \tag{10}$$

$$N + NO \rightarrow N_2 + O \tag{11}$$

Reactions (10) and (11) have been identified by van Gaens to play a significant role together in the NO loss. The rate of reaction (10) producing NO_2 increases with a decreasing gas temperature which could explain the differences observed in figure 6 between turbulent and laminar flow (see also table 1).

4.1.2. Effects of the gas curtain. A gas curtain fed by 5.0 slm dry air is added to the turbulent flow case of 3.0 slm argon + 1.0% air. Figure 6(c) depicts the NO density distribution which is compared to the case without gas curtain in figure 6(b). The gas curtain has a significant impact on the spatial distribution of the NO density. The presence of a strong decay of the NO density is observed along the axial direction. This is due to the additional gas flow from the curtain which enhances the mixing in the effluent and the far field region and reduces the gas temperature in the effluent, (table 1). The gas temperature is actually mostly affected by the curtain and will reduce thermal diffusion of NO in the laminar case. Interestingly, on the axis of symmetry, close to the nozzle, one can observe the same density. This observation corroborates the previous conclusion that NO is, in fact, mainly produced in the first millimeters in the vicinity of the nozzle. A decrease in T_{gas} leads to an enhancement of reaction (10) and the destruction of NO.

4.2. Surrounding air mixed in the effluent

Figure 8 depicts the air density derived from the fluorescence decay time constant of NO present within the effluent and far field for the conditions corresponding to figure 6. The three maps are corrected for the gas temperature variations, when the latter is known, which are dependent on the flow rate (see table 1). Starting with the laminar case with gas curtain on (figure 8(a)), one observes a smooth positive gradient along the axial direction and a very steep density gradient in the radial direction. In this case, where the flow is laminar, the diffusion process of air into the plasma effluent is enhanced by a higher temperature gradient between the effluent and the gas curtain. This has been experimentally shown in a similar jet by van Gessel *et al* [46] and by Reuter *et al* [47]. In addition, Iseni *et al* have also reported in a previous work the presence of Kelvin–Helmholtz instabilities and proposed those results from the temperature gradient [22]. The core of the effluent contains about 1% air which directly results from the fraction of air admixed to the feed gas. At 7.5 mm, the air density hardly reaches 2% and is in excellent agreement with the value measured by Raman scattering in a similar jet as reported by van Gessel *et al* [48].

Figure 8(b) shows the air density for a flow rate of 3.0 slm without gas curtain. Remarkably, the density map looks similar to the laminar case with shielding (figure 8(a)), except on one side where the gas curtain seems to force the air onto the border of the effluent. Despite the turbulent flow, which has been shown in [22], the diffusion of air in the first 5 mm is negligible o*n*-axis. This is not the case radially as shown by van Gessel *et al* [46]. It is also clear that the thermal diffusion is significantly reduced since the gas temperature is 90–30 K lower than the laminar case along the axial direction (see table 1 and figure 8(a)). The absolute value of the air distribution in a similar jet has been carried out by Dünnbier *et al* who investigated on the same plasma source the o*n*-axis diffusion of ambient species by means of MBMS complemented with fluid dynamic simulations [49]. The air concentration at 7.5 mm is measured to be 1.8% and is in excellent agreement with the present work. The results suggest that thermal diffusion in the laminar flow regime compensates for the turbulent mixing in the turbulent flow regime.

It was shown previously that switching on the gas curtain around the plasma effluent has an impact on the spatial distribution of NO (see figure 6(c)). The visualization of the enhanced mixing of the effluent with the gas curtain is presented in figure 8(c). The area containing an air density up to 1% is now reduced from 5.5–3.8 mm and is narrower than in the case with the gas curtain (figures 8(a) and (b)). The gas curtain enhances the air diffusion into the effluent which leads to an additional cooling of the gas. This result corroborates very well with the steeper NO density gradient (see figure 6(c)). Interestingly, the air density is asymmetric compared to the two other cases and can be attributed to the curtain gas device which may not have been perfectly aligned.

4.3. Influence of the substrate on the NO density distribution

In this section, the impact of a fixed substrate on the NO density distribution is studied. While previously the plasma jet and its effluent ran free into an open atmosphere, for most applications a substrate is present. A stainless-steel plate, grounded to avoid any charge accumulation on the surface, is fixed at a distance of 7.5 mm from the nozzle. LIF is performed as previously described and the recorded signal is corrected for vignetting during post-processing. For both

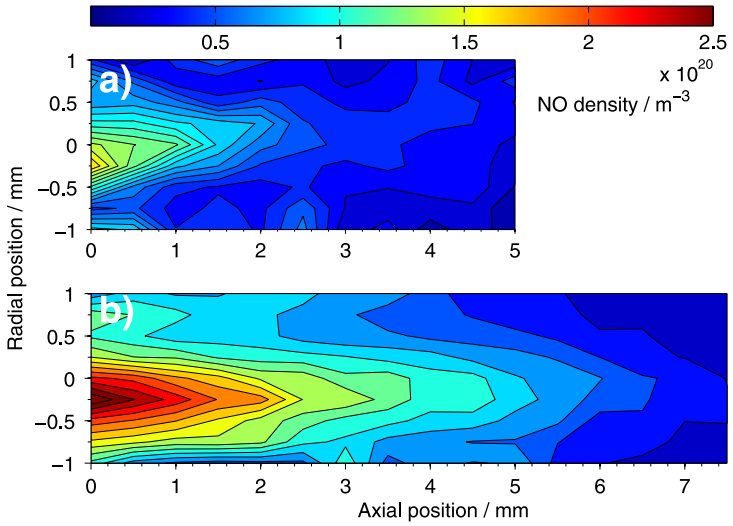

Figure 9. Absolute NO densities, measured without gas curtain in a turbulent (a) and with gas curtain in laminar (b) flow rate regime. A substrate is placed at a distance of 7.5 mm from the nozzle. The input power is supposed to be constant and identical as the previous measurements. The two maps have different lengths because it was not possible to obtain a significant signal-to-noise ratio in the turbulent case in the vicinity of the substrate. This issue is enhanced by the vignetting and higher density of quenchers (air) near the substrate surface.

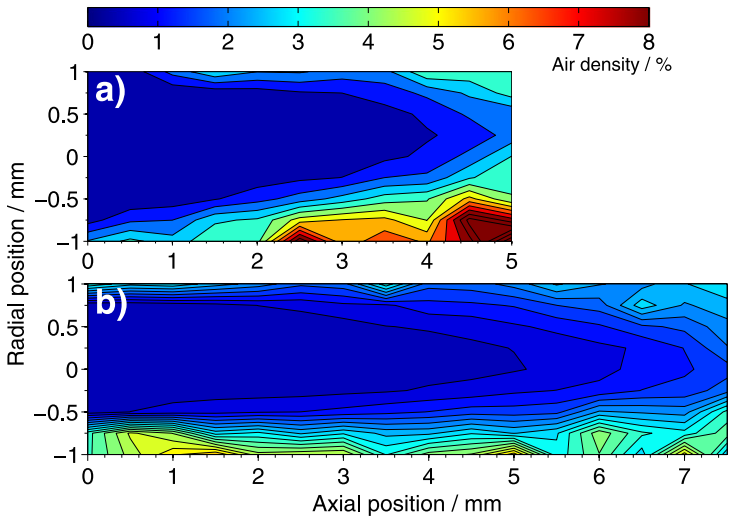

Figure 10. Air density distribution determined from the temporal evolution of the NO fluorescence. The corresponding NO densities are shown in figure 9. (a) and (b) depict the air density distribution for the turbulent case and for the laminar case respectively.

regimes (laminar and turbulent) 1.0 slm and 3.0 slm argon with 1.0% air admixed are applied with a gas curtain of 1.7 slm and 5.0 slm respectively. The results are depicted in figure 9. Significant differences in NO density profiles between the laminar and the turbulent case are observed. In the laminar case, the symmetry of the NO density profile is well conserved from the nozzle to the substrate whereas the pattern in the turbulent case appears to be asymmetric. The more distorted NO density profile shown in figure 9(a) beyond doubt is due to the

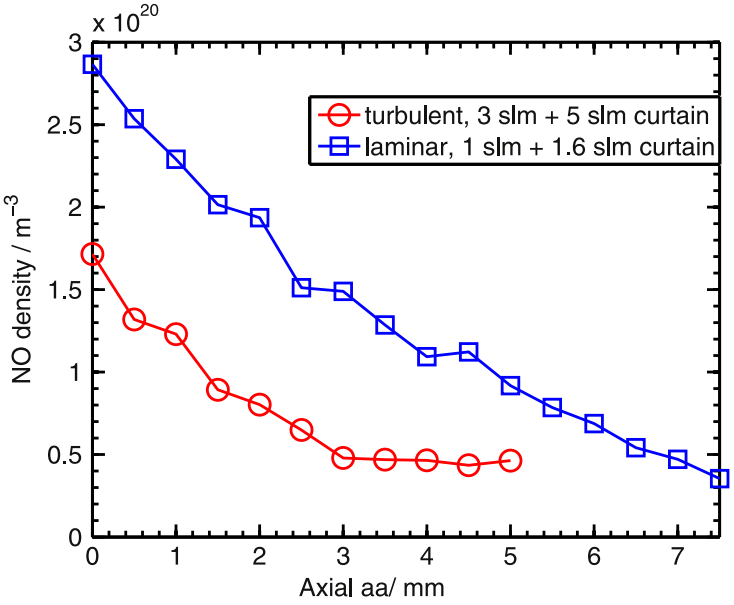

Figure 11. Absolute NO density along the axial position. The substrate is positioned at 7.5 mm from the nozzle.

turbulence which is enhanced by a natural back reflection of the flow on the substrate. figure 10 presents the air density distribution when the plate is present. As expected, figure 10(a), which corresponds to the turbulent flow case, shows a higher air density on one corner of the probed domain. This confirms the recycling pattern induced by the plate and enhances the mixing of the effluent with the ambient air. The argon flux keeps a quasi-symmetrical structure as without the plate and does not seem to drag more air into the effluent up to 4.0 mm. The axial dependence of the NO density is not easily readable on the color-map in figure 9. To this end, an additional plot of the maxima along the axial direction is shown in figure 11. In both cases, the NO density decreases linearly with the same slope from 0–3.0 mm from the nozzle. The density decay results from the diffusion either thermal or turbulent dominating but produces the same reduction of the NO density over the first 3 mm. Interestingly, from 3.0–5.0 mm with turbulent flow, the density remains constant. It is stressed that the detection limit (about 2×10^{19} m^{-3}) was not reached in these measurements.

4.4. MBMS measurement of NO and O_3 densities: comparison with the LIF

Absolute densities of NO and O_3 have been measured by MBMS. The NO density will be compared to the densities determined by LIF in this section. The experimental conditions are identical to the ones used during the LIF measurement for the turbulent regime, 3 slm feed gas flow rate, 5 slm dry air as a gas curtain. It is emphasized that the plasma was not coupled or corrected to the MBMS plate containing the sampling orifice, which resulted in a significant increase of the current and luminous intensity easily noticeable with the naked eye.

4.4.1. NO and O_3 densities. Figure 12 depicts the results of the MBMS measurement for NO and O_3 densities at 7.5 mm from the jet nozzle. Quantitatively, densities measured by MBMS as well as LIF are in the same order of magnitude in spite of a factor 5 difference between both techniques. A discussion dealing with this discrepancy is developed in section 4.4.2.

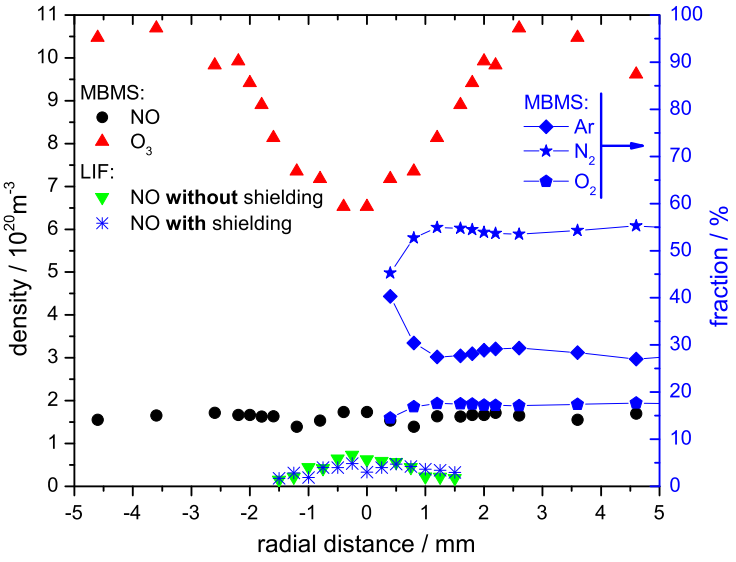

Figure 12. Radial absolute density profiles of the NO and O_3 measured by MBMS and LIF (left axis) and the absolute Ar, N_2 and O_2 fraction (right axis) from MBMS. The sampling orifice of the MBMS is 7.5 mm way from the jet nozzle. The plasma jet is fed with argon plus 1.0% air admixture and the deposited power into the plasma is similar for each measurement set with maximum 15% variation.

Interestingly, the density of NO measured on the axis of symmetry by MBMS (figure 12) is identical to the maximum of the NO density map measured by LIF in figure 9. The density is found to be $1.8 \times 10^{20}\,\mathrm{m}^{-3}$.

Moreover, the MBMS recorded signal at mass 30 u (atomic mass unit) corresponds to a nearly constant NO density along the radial position which is not likely to be the case. In comparison with the LIF data, the trend in the radial direction from 0.0 mm to 1.0 mm are identical: the maximum density is at the axis of symmetry. A spatial resolution difference of the MBMS compared to the LIF might explain the slight shift of the position of the maximum. To be sure that the resolution limit was not reached, the response of the signal at 30 u has been checked by adding 0.2% air admixture instead of 1.0% initially. The result is a drop of the counts by 40%. According to the work of van Gessel *et al* [16] on a similar plasma source, the production of NO with regard to the air admixture is strongly affected and the experimental results confirm the same trend. Consequently, the signal at mass 30 is clearly reflecting the N_xO_y production from the plasma jet. A scan at mass 46, which corresponds to the NO_2 mass, is systematically performed and no variation is observed compared to the recorded background.

The interaction of the flow and the wall of the cup-like structure (in which the sampling orifice is located at the bottom) can act as a reservoir and influence the samples. Figure 12 shows on the right axis the fraction of Ar, N_2 and O_2 along the radial distance at 7.5 mm axial distance from the nozzle. A direct comparison with the air density profile in figure 10(a) can be partially made since the latter presents the first 5.0 mm of the effluent. However, a strong increase of N_2 and O_2 is expected due to the turbulent diffusion also known as eddy diffusion. Moreover, as mentioned in section 4.2, the air densities determined by LIF are in agreement with the value found in the literature. The MBMS density measurements of O_2 are in the order of 17% at 7.5 mm (figure 12) and are in excellent agreement with the Raman scattering

Table 2. Quantification of the maximum N_xO_y densities in the effluent at 7.5 mm from the nozzle of the kinpen. The data are either from this work (NO) or estimated from the literature [26, 51].

molecule	NO	NO_2	HNO_2	HNO_3	N_2O	N_2O_5
max. density / 10^{19} molecule m^{-3}	5.3	2.0	≈0.9	≈0.6	≈4	$\lessapprox$0.1

measurements published in [48] at the same distance from the nozzle. Although an exhaust system has been implemented to keep the partial air pressure close to the free-field situation, an accumulation of air and argon occurs and leads to a recycling pattern as described by van Ham *et al* [25] which is partially visible in figure 10. This recycling pattern increases the residence time of N_xO_y species, enhances the oxidation of NO and contributes to the signal at 30 u as discussed further. In addition, it was observed during the measurement that by positioning the plasma jet 10.0 mm off-axis from the sampling orifice, the signal at 30 u reaches the level of the background recording.

The shape of the ozone density profile may be mainly by the larger residence time due to the above mentioned recycling pattern. The formation of ozone is known to result merely from a three body reaction involving molecular and atomic oxygen up to a temperature slightly above room temperature [45]. The dip in the center could be enhanced by a higher atomic oxygen density which quenches ozone efficiently [50].

4.4.2. Discussion. The fact that the NO density determined by the MBMS is significantly higher than the one obtained with LIF has already been reported in [25]. The authors would argue that the high electron energy of the MBMS ion source (maximum peak distribution at 70 eV) will dissociate any NO containing molecules (N_xO_y). For the kinpen, several experimental investigations have been reported on the net production rates of N_xO_y although in different flow conditions [26], HNO_3 [51], N_2O_5 [52]. In addition, Pipa and Röpcke, who have reported the measurements of the latter species, have also measured net production rates of N_2O and HNO_2 [18]. However, they used a different source and as the authors do not report any detection of ozone, it hints that the plasma source has a significantly higher gas temperature than the kinpen [19]. At present, the absolute net production rate of R_{NO_2} (expressed in molecules per second, molecule $\cdot$ s^{-1}) has been published for identical conditions (3 slm Ar with 1.0% air admixture and 5 slm curtain gas) and yields a net production rate of R_{NO_2}= 2.2×10^{15} molecule $\cdot$ s^{-1} [26]. Note that Verreycken measured OH radicals in the visible effluent by LIF and UV absorption and reported a concentration of 1.5×10^{21} m^{-3} 1.0 mm distance from the nozzle but for a gas flow rate of 4.0 slm with 1.3% water admixture [53]. Winter *et al* could determine the ozone concentration spatially resolved (starting from 4.0 mm from the nozzle tip) of 1.5×10^{22} m^{-3} at 4.0 mm axial distance with a argon flow rate of 3.0 slm and 1.0% oxygen admixture [54]. The formation of NO_2 already occurs within the effluent resulting from the oxidation of NO by atomic oxygen. In the case when the maximum gas temperature does not exceed significantly the room temperature, ozone formation will occur and lead to the efficient oxidation of NO within the effluent. The results of the kinetic model of van Gaens *et al* report on the formation of N_2O molecules which occurs in parallel to the NO generation. Recently, this N_2O has been detected in the far field beyond the visible plume of the kinpen [55]. In other words, N_2O is already produced in the vicinity of the electrodes. Interestingly, the production of

N_2O seems to reach a steady-state at the tip of the nozzle and yields a density slightly below the NO density. Table 2 shows the estimation of maximum densities of N_xO_y at 7.5 mm from the nozzle of the plasma jet susceptible to dissociation within the MBMS chamber by the ionization source. In spite of the data being all from the same plasma source (kinpen) the experimental conditions may differ. In the work reported in [26, 51], the plasma jet operates with a different surrounding atmosphere and blows into a multipass cell which is pumped down or at atmospheric pressure. These conditions are dissimilar from the experimental environment of the cup-like structure of the MBMS. Although the cracking patterns of some of the molecules given in table 2 remain unclear, N_2O and NO_2 have been identified to contribute by 25% and 60% respectively to 30 u [32]. As a consequence, both molecules are the most dominant secondary species which contribute to the NO signal at mass 30 u together with NO. This could lead to an overestimation of the NO density by about 50% in the present work when assuming the densities in table 2.

5. Conclusion

In this work, LIF was used to measured the absolute and spatially resolved NO density in the effluent of an argon RF cold plasma jet operating under atmospheric conditions in laminar and turbulent flow regimes. The LIF signal is absolutely calibrated with a known reference density of NO. Furthermore, a characterization of the vignetting induced by a substrate is performed. It is reported that NO is dominantly produced within the first part of the effluent and reaches a maximum of 2.5×10^{20} molecule. cm^{-3} and 1.7×10^{20} molecule. cm^{-3} at the jet nozzle for the laminar and turbulent flow case respectively. The gas temperature measured by LIF is higher in the laminar case than in the turbulent case by about 100 K at the nozzle. The temperature difference is argued to be the main cause of the different NO density. The absolute air density spatially resolved in the effluent was determined from the quenching of the NO fluorescence. The diffusion of air in the Ar effluent is mostly thermally driven in the laminar case whereas turbulent diffusion is responsible for the mixing with the ambient in a turbulent regime. Remarkably, both conditions lead to a similar spatial distribution of air within the jet effluent. Moreover, the gas curtain applied around the effluent appears not to affect the NO density close to the nozzle but enhances the diffusion of air into the effluent without affecting the visible emission length of the effluent. The air concentrations are in excellent agreement with the data obtained by other techniques reported in the literature [46, 47]. The maximum air density reaches about 4–7% and 2% at 7.5 mm from the nozzle respectively with and without gas curtain in the turbulent case. The NO lifetime decays faster due to an enhancement of the oxidation induced by atomic oxygen and ozone from the plasma which leads to the production of NO_2. The latter is assumed to play a role in a chemical recycling reaction in the effluent zone to form NO again. This reaction is gas temperature dependent.

Furthermore, measurements have been performed with an absolutely calibrated MBMS. The comparison of both techniques (LIF and MBMS) are in the same order of magnitude around 5×10^{19}–15×10^{19} molecule. cm^{-3}on the axial symmetry at 7.5 mm. The non-selectivity of the MBMS induces measurements which overestimate the NO density resulting from a significant contribution to the NO_2 and N_2O molecules generated in the effluent. An additional effect of the flow cannot be excluded and could contribute to the discrepancies.

Acknowledgments

This work was supported by the MPNS COST-Action MP1101 and the data was obtained during a Short-Term Scientific Mission (STSM) of SI at the TU/e Eindhoven University of Technology. PB would like to acknowledge the support of the Dutch Technology Foundation (STW), the University of Minnesota and the DOE Plasma Science Center. SH acknowledges the support of the Foundation for Fundamental Research on Matter (FOM). SI thanks Ansgar Schmidt-Bleker for the fruitful conversations. SI and SR thank the BMBF for supporting the ZIK plasmatis and the Leibniz Institute for Plasma Science and Technology (INP Greifswald e. V.) grant number 03Z2DN12.

References

[1] Lu X, Laroussi M and Puech V 2012 On atmospheric-pressure non-equilibrium plasma jets and plasma bullets *Plasma Sources Sci. Technol.* **21** 034005
[2] Samukawa S *et al* 2012 The 2012 plasma roadmap *J. Phys. D: Appl. Phys.* **45** 253001
[3] von Woedtke T, Reuter S, Masur K and Weltmann K D 2013 Plasmas for medicine *Phys. Rep.* **530** 291–320
[4] Kong M G, Kroesen G, Morfill G, Nosenko T, Shimizu T, van Dijk J and Zimmermann J L 2009 Plasma medicine: an introductory review *New J. Phys.* **11** 115012
[5] Ehlbeck J, Schnabel U, Polak M, Winter J, von Woedtke T, Brandenburg R, von dem Hagen T and Weltmann K D 2011 Low temperature atmospheric pressure plasma sources for microbial decontamination *J. Phys. D: Appl. Phys.* **44** 013002
[6] van Gils C A J, Hofmann S, Boekema B K H L, Brandenburg R and Bruggeman P J 2013 Mechanisms of bacterial inactivation in the liquid phase induced by a remote rf cold atmospheric pressure plasma jet *J. Phys. D: Appl. Phys.* **46** 175203
[7] Laroussi M, Karakas E and Hynes W 2011 Influence of cell type, initial concentration, and medium on the inactivation efficiency of low-temperature plasma *IEEE Trans. Plasma Sci.* **39** 2960–1
[8] Lademann J, Richter H, Schanzer S, Patzelt A, Thiede G, Kramer A, Weltmann K D, Hartmann B and Lange-Asschenfeldt B 2012 Comparison of the antiseptic efficacy of tissue-tolerable plasma and an octenidine hydrochloride-based wound antiseptic on human skin *Skin Pharmacol. Physiol.* **25** 100–6
[9] Matthes R, Bekeschus S, Bender C, Koban I, Hubner N O and Kramer A 2012 Pilot-study on the influence of carrier gas and plasma application (open resp. delimited) modifications on physical plasma and its antimicrobial effect against pseudomonas aeruginosa and staphylococcus aureus *GMS Krankenhhyg. Interdiszip.* **7** Doc02
[10] Nosenko T, Shimizu T and Morfill G E 2009 Designing plasmas for chronic wound disinfection *New J. Phys.* **11** 115013
[11] Graves D B 2012 The emerging role of reactive oxygen and nitrogen species in redox biology and some implications for plasma applications to medicine and biology *J. Phys. D: Appl. Phys.* **45** 263001
[12] Bekeschus S, Kolata J, Winterbourn C, Kramer A, Turner R, Weltmann K D, Bröker B and Masur K 2014 Hydrogen peroxide: a central player in physical plasma-induced oxidative stress in human blood cells *Free Radic. Res.* **48** 542–9
[13] Bundscherer L, Wende K, Ottmuller K, Barton A, Schmidt A, Bekeschus S, Hasse S, Weltmann K D, Masur K and Lindequist U 2013 Impact of non-thermal plasma treatment on MAPK signaling pathways of human immune cell lines *Immunobiology* **218** 1248–55
[14] Barekzi N and Laroussi M 2013 Effects of low temperature plasmas on cancer cells *Plasma Process. Polym.* **10** 1039–50
[15] Lancaster J 1996 *Nitric Oxide: Principles and Actions* (New York: Academic)

[16] van Gessel A F H, Alards K M J and Bruggeman P J 2013 NO production in an RF plasma jet at atmospheric pressure *J. Phys. D: Appl. Phys.* **46** 265202
[17] van Gessel A F H, Hrycak B, Jasiński M, Mizeraczyk J, van der Mullen J J A M and Bruggeman P J 2013 Temperature and NO density measurements by LIF and OES on an atmospheric pressure plasma jet *J. Phys. D: Appl. Phys.* **46** 095201
[18] Pipa A V and Ropcke J 2009 Analysis of the mid-infrared spectrum of the exhaust gas from an atmospheric pressure plasma jet (APPJ) working with an argon air mixture *IEEE Trans. Plasma Sci.* **37** 1000–3
[19] Pipa A V, Reuter S, Foest R and Weltmann K D 2012 Controlling the NO production of an atmospheric pressure plasma jet *J. Phys. D: Appl. Phys* **45** 085201
[20] Stoffels E, Gonzalvo Y A, Whitmore T D, Seymour D L and Rees J A 2006 A plasma needle generates nitric oxide *Plasma Sources Sci. Technol.* **15** 501–6
[21] Stoffels E, Aranda Gonzalvo Y, Whitmore T D, Seymour D L and Rees J A 2007 Mass spectrometric detection of short-living radicals produced by a plasma needle *Plasma Sources Sci. Technol.* **16** 549–56
[22] Iseni S, Schmidt-Bleker A, Winter J, Weltmann K D and Reuter S 2014 Atmospheric pressure streamer follows the turbulent argon air boundary in a MHz argon plasma jet investigated by OH-tracer plif spectroscopy *J. Phys. D: Appl. Phys.* **47** 152001
[23] Robert E, Sarron V, Darny T, Riès D, Dozias S, Fontane J, Joly L and Pouvesle J M 2014 Rare gas flow structuration in plasma jet experiments *Plasma Sources Sci. Technol.* **23** 012003
[24] Reuter S, Winter J, Schmidt-Bleker A, Tresp H, Hammer M U and Weltmann K D 2012 Controlling the ambient air affected reactive species composition in the effluent of an argon plasma jet *IEEE Trans. Plasma Sci.* **40** 2788–94
[25] van Ham B, Hofmann S, Brandenburg R and Bruggeman P J 2014 *In situ* absolute air, O_3 and NO densities in the effluent of a cold RF argon atmospheric pressure plasma jet obtained by molecular beam mass spectrometry *J. Phys. D: Appl. Phys.* **47** 224013
[26] Iseni S, Reuter S and Weltmann K D 2014 NO_2 dynamics of an ar air plasma jet investigated by *in situ* quantum cascade laser spectroscopy at atmospheric pressure *J. Phys. D: Appl. Phys.* **47** 075203
[27] Winter J, Wende K, Masur K, Iseni S, Dnnbier M, Hammer M U, Tresp H, Weltmann K-D and Reuter S 2013 Feed gas humidity: a vital parameter affecting a cold atmospheric-pressure plasma jet and plasma-treated human skin cells *J. Phys. D: Appl. Phys.* **46** 295401
[28] Tamura M, Berg P A, Harrington J E, Luque J, Jeffries J B, Smith G P and Crosley D R 1998 Collisional quenching of CH(A), OH(A), and NO(A) in low pressure hydrocarbon flames *Combust. Flame* **114** 502–14
[29] Hazama H, Fujiwara M and Tanimoto M 2000 Removal processes of nitric oxide along positive streamers observed by laser-induced fluorescence imaging spectroscopy *Chem. Phys. Lett.* **323** 542–8
[30] Heard D E, Jeffries J B and Crosley D R 1991 Collisional quenching of $A^2\Sigma^+$NO and $A^2\Delta$CH in low pressure flames *Chem. Phys. Lett.* **178** 533–7
[31] Verreycken T, van der Horst R M, Sadeghi N and Bruggeman P J 2013 Absolute calibration of oh density in a nanosecond pulsed plasma filament in atmospheric pressure He−H_2O: comparison of independent calibration methods *J. Phys. D: Appl. Phys.* **46** 464004
[32] Stein S E 2014 Mass Spec Data Center *NIST Chemistry WebBook* (*NIST Standard Reference Database No* 69) ed P J Linstrom and W G Mallard (Gaithersburg, MD: National Institute of Standards and Technology)
[33] Hofmann S, van Gils K, van der Linden S, Iseni S and Bruggeman P 2014 Time and spatial resolved optical and electrical characteristics of continuous and time modulated rf plasmas in contact with conductive and dielectric substrates *Eur. Phys. J.* D **68** 56
[34] Bruggeman P J, Sadeghi N, Schram D C and Linss V 2014 Gas temperature determination from rotational lines in non-equilibrium plasmas: a review *Plasma Sources Sci. Technol.* **23** 023001
[35] van Gessel A F H and Bruggeman P J 2013 Thermalization of rotational states of NOA$(2)\Sigma^+(v = 0)$ in an atmospheric pressure plasma *J. Chem. Phys.* **138** 204306

[36] Nguyen T D and Sadeghi N 1983 Rotational and vibrational distributions of N2($C^3\Pi_u$) excited by state-selected Ar($^3P_2$) and Ar($^3P_0$) metastable atoms *Chem. Phys.* **79** 41–55
[37] van Gessel A F H, Hrycak B, Jasinski M, Mizeraczyk J, van der Mullen J J A M and Bruggeman P J 2012 Temperature fitting of partially resolved rotational spectra *J. Instrum.* **7** C02054
[38] Raiche G A and Crosley D R 1990 Temperature dependent quenching of the $A^2\Sigma^+$ and $B^2\Pi$ states of NO *J. Chem. Phys.* **92** 5211
[39] Drake M C and Ratcliffe J W 1993 High-temperature quenching cross-sections for nitric-oxide laser-induced fluorescence measurements *J. Chem. Phys.* **98** 3850–65
[40] Stuart McDermid I and Laudenslager J B 1982 Radiative lifetimes and electronic quenching rate constants for single-photon-excited rotational levels of NO($A^2\Sigma^+$, $v' = 0$) *J. Quant. Spectrosc. Radiat. Transfer* **27** 483–92
[41] Paul P H, Gray J A, Durant J L and Thoman J W 1996 Collisional electronic quenching rates for NOA(2)$\Sigma^+(v' = 0)$ *Chem. Phys. Lett.* **259** 508–14
[42] Fricke K, Reuter S, Schroder D, Schulz-von der Gathen V, Weltmann K D and von Woedtke T 2012 Investigation of surface etching of poly (ether ether ketone) by atmospheric-pressure plasmas *IEEE Trans. Plasma Sci.* **40** 2900–11
[43] Ellerweg D, Benedikt J, von Keudell A, Knake N and Schulz-von der Gathen V 2010 Characterization of the effluent of a He/O_2 microscale atmospheric pressure plasma jet by quantitative molecular beam mass spectrometry *New J. Phys.* **12** 013021
[44] van Gaens W, Bruggeman P J and Bogaerts A 2014 Numerical analysis of the NO and O generation mechanism in a needle-type plasma jet *New J. Phys.* **16** 063054
[45] Fridman A 2008 *Plasma Chemistry* (Cambridge: Cambridge University Press)
[46] van Gessel B, Brandenburg R and Bruggeman P 2013 Electron properties and air mixing in radio frequency driven argon plasma jets at atmospheric pressure *Appl. Phys. Lett.* **103** 064103
[47] Reuter S, Winter J, Schmidt-Bleker A, Schroeder D, Lange H, Knake N, Schulz-von der Gathen V and Weltmann K D 2012 Atomic oxygen in a cold argon plasma jet: talif spectroscopy in ambient air with modelling and measurements of ambient species diffusion *Plasma Sources Sci. Techno.* **21** 024005
[48] van Gessel A F H, van Grootel S C and Bruggeman P J 2013 Atomic oxygen talif measurements in an atmospheric-pressure microwave plasma jet within situxenon calibration *Plasma Sources Sci. Technol.* **22** 055010
[49] Dünnbier M, Schmidt-Bleker A, Winter J, Wolfram M, Hippler R, Weltmann K D and Reuter S 2013 Ambient air particle transport into the effluent of a cold atmospheric-pressure argon plasma jet investigated by molecular beam mass spectrometry *J. Phys. D: Appl. Phys.* **46** 435203
[50] Zhang S, van Gessel A F H, van Grootel S C and Bruggeman P J 2014 The effect of collisional quenching of the O $3p^3P_J$ state on the determination of the spatial distribution of the atomic oxygen density in an APPJ operating in ambient air by TALIF *Plasma Sources Sci. Technol.* **23** 025012
[51] Schmidt-Bleker A, Winter J, Iseni S, Dünnbier M, Weltmann K D and Reuter S 2014 Reactive species output of a plasma jet with a shielding gas devicecombination of FTIR absorption spectroscopy and gas phase modelling *J. Phys. D: Appl. Phys.* **47** 145201
[52] Reuter S, Winter J, Iseni S, Schmidt-Bleker A, Dünnbier M, Masur K, Wende K and Weltmann K 2014 The influence of feed gas humidity versus ambient humidity on atmospheric pressure plasma jet-effluent chemistry and skin cell viability *IEEE Trans. Plasma Sci.* doi:10.1109/TPS.2014.2361921
[53] Verreycken T, Mensink R, van der Horst R, Sadeghi N and Bruggeman P J 2013 Absolute OH density measurements in the effluent of a cold atmospheric-pressure Ar-H_2O RF plasma jet in air *Plasma Sources Sci. Technol.* **22** 055014
[54] Winter J, Dünnbier M, Schmidt-Bleker A, Meshchanov A, Reuter S and Weltmann K D 2012 Aspects of UV-absorption spectroscopy on ozone in effluents of plasma jets operated in air *J. Phys. D: Appl. Phys.* **45** 385201
[55] Schmidt-Bleker A 2014 private communication